JOURNAL OF MATERIALS SCIENCE 28 (1993) 2808–2814

Properties of electron-beam-welded and laser-welded austenitic Fe–28Mn–5Al–1C alloy

JIN-SON KU, NEW-JIN HO AND SIE-CHIN TJONG*
Institute of Materials Science and Engineering, National Sun Yat-Sen University, Kaohsiung, Taiwan

Austenitic Fe–28Mn–5Al–1C alloy was welded by electron-beam and CW CO_2 laser techniques. Tensile tests, impact tests, potentiodynamic and cyclic polarization measurements were used to evaluate the mechanical properties and corrosion behaviour of the weld materials. Metallographic examination showed that the microstructure of the electron-beam-welded and laser-welded metals consisted mainly of the columnar and equiaxed austenitic structures. Grain growth in the heat-affected zone (HAZ) was minimal for welding with these two techniques. The tensile and impact tests indicated that the weld materials exhibited lower tensile strength, percentage elongation, percentage reduction in area and impact energy than those of the base alloy. The polarization measurements revealed that the anodic polarization behaviour of the HAZs of the electron-beam-welded and laser-welded materials was identical to that of the base alloy when exposed in 1M Na_2SO_4 solution. However, the electron-beam-welded and laser-welded metals exhibited a higher current density in the passive region than that of the base alloy when exposed to 1N H_2SO_4 acid solution.

1. Introduction

There are several reasons why manganese and aluminium can be suitable as possible substitutes for nickel and chromium, respectively, in conventional Fe–Cr–Ni stainless steels. They are both cheap and abundant, and manganese, particularly, has been used in stainless steels before [1, 2]. Moreover, chromium is considered as a strategic element for most countries [3]. Fe–Mn–Al–C alloys, with nickel replaced by manganese and chromium replaced by aluminium, have attracted considerable attention recently. The Fe–Mn–Al–C alloys have been shown to exhibit a high-strength-to-weight ratio, good oxidation resistance and excellent mechanical properties at low temperatures but poor aqueous corrosion resistance [4–8].

Carbon is generally known to be an effective austenite stabilizer which, together with manganese, has the capability of retaining the face-centred-cubic austenitic structure at room temperature. Hence, an optimum composition of manganese, aluminium and carbon (e.g. 25–30% Mn, 8–10% Al and 1% C) should produce an austenitic alloy with good physicomechanical properties [9]. The oxidation properties [4, 6, 10–12], aqueous corrosion behaviour [8, 13, 14], mechanical properties [15, 16, 17, 18] and phase transformation [14, 19] of Fe–Mn–Al–C alloys based on compositions of Fe–30Mn–(8–10)Al–(0.4–1)C have been investigated by Tjong and his co-workers extensively. As the Fe–Mn–Al–C alloys are developed for usage in industrial applications, the weldability of these alloys must be assessed. This is because failure in fabricated engineering structures often initiates at welded joints.

The microstructure of the Fe–Mn–Al–C alloys depends greatly on the carbon content. It has been reported that the addition of 1 wt% of carbon to a Fe–30Mn–9Al alloy leads to the formation of a fully austenitic structure [13, 14]. As the carbon content is decreased to 0.4 wt %, the microstructure of the Fe–30Mn–10Al alloy consists of both austenitic and ferritic phases [15]. Therefore, the carbon content plays a major role in controlling the microstructure of the weld metal. Aidun and co-workers [20, 21] reported that the austenite content in the weld metal of the Fe–Mn–Al–C alloys depends on the chemistry of the alloys, i.e. the amount of austenite increases with increasing carbon content in the alloys. The different types of ferrite and other constituents were identified. A similar result was also reported by Chou and Lee [22, 23]. They pointed out that the welding heat input has a strong influence on the amount of residual ferrite in the weld metal [24]. The heat input in gas-tungsten arc (GTA) processes typically varied from 270 to 1466 J mm^{-1} [24] Moreover, major cracks occurred in the weld metal and some cracks propagated along the coarsened austenitic grains in the heat-affected zone (HAZ) after Varestraint testing. Ferrite in the weld metal exhibited beneficial effects in reducing weld cracking [23]. On the other hand, laser and electron-beam (EB) welding are particularly suited to Fe–Mn–Al–C alloys because the heat input is considerably lower than in arc processes. It is desirable to

* Present address: Department of Applied Science, City Polytechnic of Hong Kong, 83 Tat Chee Avenue, Kowloon, Hong Kong

0022–2461

weld Fe–Mn–Al–C alloys with lower heat input to avoid grain growth in the HAZs. Furthermore, since there is no electrode employed in laser and EB welding, the HAZ and the weld are extremely narrow. Consequently, the distortion resulting from welding is small and the induced residual stresses are very low in the HAZ. In this paper, we give a first report on the mechanical properties and corrosion behaviour of the EB welded and laser welded austenitic Fe–28Mn–5Al–1C alloy.

2. Experimental procedure

2.1. Alloy Preparation

Austenitic Fe–28Mn–5Al–1C alloy was prepared in a laboratory induction furnace followed by ingot casting and hot rolling. The chemical composition of the alloy investigated is tabulated in Table I. The plates were solution treated at 1050 °C for 2 h and subsequently oil quenched to eliminate any hot-rolled effect.

2.2. Preparation of welded specimens

The solution-treated Fe–28Mn–5Al–1C alloy was welded with a 3 kW (Torvac CVE63B) EB welder. Full penetration welds were made in 16 mm thick plates by a close-square butt-joint technique with the following parameters:

Potential	60 kV
Current	40 mA
Welding speed	20 mm s^{-1}
Chamber pressure	8×10^{-5} torr
	(1 torr = 133 Pa)

The solution-treated plates (10 mm thick) were also welded with a 3 kW (PRC FH-3000) CO_2 laser. Owing to the limited power available, the weld runs had to be carried out from opposite sides to obtain complete penetration. The focal point was positioned 1 mm inside the specimen. The following welding parameters were employed:

Laser power	12.6 kW
Welding speed	8.3 mm s^{-1}
Shielding gas	Helium
Helium gas flow	0.6 l s^{-1}
Defocus length	1 mm

2.3. Preparation of mechanical test specimens

Axial cyclindrical tensile-test specimens of 20 mm gauge length and of 5 mm diameter were machined from the solution-treated plates with their lengths parallel to the rolling direction. Specimens of identical dimensions were also prepared from the EB and laser-welded plates with the weld metals located in the central portion of the gauge length and transverse to the specimen axis. All-weld tensile specimens could not be obtained because the EB and laser-welded metals are much finer than those obtained by the GTA process.

Charpy impact-test specimens ($10 \times 55 \times 5$ mm^3) were cut from the solution-treated plates, EB welded and laser-welded plates, respectively. For the welded specimens, notches were located in the weld metals.

TABLE I Chemical composition of the Fe–28Mn–5Al–1C alloy (wt %)

C	P	S	Si	Mn	Al	Fe
1.04	0.04	0.011	0.24	28.3	5.38	Balance

2.4. Preparation of potentiodynamic test specimens

Specimens for potentiodynamic measurements were in the form of a disc (11 mm diameter, 5 mm thick). The discs were cut from the solution-treated Fe–28Mn–5Al–1C alloy, weld metals, and HAZs of the EB welded and laser-welded plates, respectively. The disc was ground with SiC paper down to 800 grit.

2.5. Mechanical tests

Tensile tests were conducted at room temperature with an Instron universal testing machine model 1125. After testing, the fracture surface was ultrasonically cleaned in acetone and subsequently examined in a scanning electron microscope (SEM, JEOL model JSM-820 equipped with a Link AN 10/85S EDAX system). Charpy impact tests were conducted at 23, − 40, − 60 and − 196 °C, respectively by using a Shimadzu impact tester.

2.6. Potentiodynamic and cyclic polarization measurements.

The test solutions used for the potentiodynamic scans were 1N H_2SO_4 and 1M Na_2SO_4 respectively. The sulphuric acid and sodium sulphate solutions were purged with nitrogen during the tests. A Princeton Applied Research (PAR) model 273 potentiostat and a personal computer equipped with PAR model 342 software were used for the measurements. A saturated calomel electrode (SCE) was used as the reference electrode and two graphite electrodes were employed as auxiliary electrodes. The existing air-formed film was removed by applying a cathodic potential of − 160 mV relative to the actual corrosion potential. The potentiodynamic scan was then initiated at this cathodic potential and scanned continuously in the anodic direction at 0.2 mV s^{-1}.

For the cyclic polarization test, the specimen was immersed in deaerated 0.5% NaCl solution for 1 h until its open-circuit potential reached a steady state. The scan was then initiated at the corrosion potential and scanned in the noble direction at a scan rate of 0.2 mV s^{-1}. When the current density reached 5×10^3 uA cm^{-2}, the scanning direction was reversed toward the more active potentials.

3. Results and discussion

3.1. Analysis of microstructure

Fig. 1a shows a typical macrostructure of the EB weldment; the microstructure of this weldment is shown in Fig. 1b. A higher magnification of the weld metal and weld-metal/HAZ are shown in Figs 2a and 2b, respectively. It can be seen that the microstructure of the weld metal consists mainly of dendritic austenite. Moreover, grain growth in the HAZ is restricted. In the EB-melted zone the metal is heated to a temperature above the melting point and is rapidly resolidified. Careful examination of the micrographs reveals that the columnar dendrites are formed near the outer part of the weld pool and equiaxed dendrites are formed near the central portion of the weld metal. During the solidification process, there is usually a partitioning of solute atoms ahead of the solid–liquid interface. This partitioning tends to produce geometric instabilities, resulting in dendritic solidification. Savage *et al.* [25] indicated that the equiaxed dendritic structure was observed in the central portion of the weld metal, due to sufficient supercooling. Furthermore, microsegregation was unavoidable in the solidification process produced by welding [25]. The steep temperature gradient associated with EB welding tended to promote the formation of columnar dendrites in the outer part of the weld. Final solidification at the central crater was associated with rapid crystal growth. The chemical compositions of the base alloy and weld metal were analysed by an energy dispersive spectroscopy (EDX) analyser attached to the SEM. The results showed that the base alloy consisted of 6.80 wt % Al, 28.21 wt % Mn and 64.99 wt % Fe. The chemical compositions of the weld metal at positions A and B shown in Fig. 1a consisted of 6.12 wt % Al, 28.19 wt % Mn, 65.69 wt % Fe, and 6.37 wt % Al, 28.29 wt % Mn, 65.34 wt % Fe, respectively. There is a slight difference in the aluminium content of the base alloy obtained by EDX and that listed in Table I. The chemical composition of the base alloy tabulated in Table I was obtained by wet chemical analysis. However, the carbon content could not be obtained in an EDX analyser attached with a Be window. Based on the EDX results, microsegregation did not occur in the weld metal during the solidification process; this is possibly due to the very short time that the weld metal remained in the molten state.

Chou and Lee [26] indicated that the *K*-phase $(FeMn)_3AlC_x$ carbides were precipitated in the austenitic phase of the weld metal of the Fe–29.5Mn–9Al alloy produced by GTA welding. The structure of these small carbide particles were observed by transmission electron microscopy (TEM). It has been re-

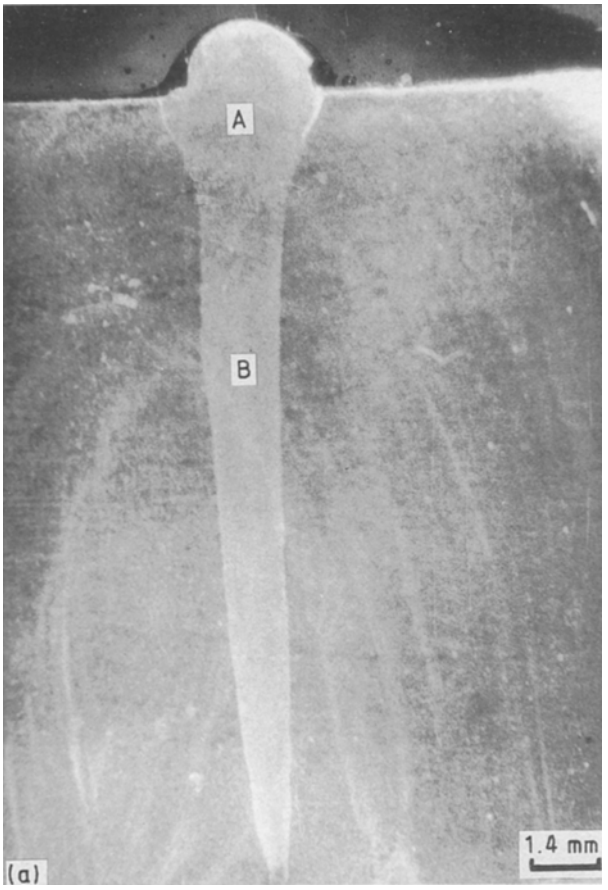

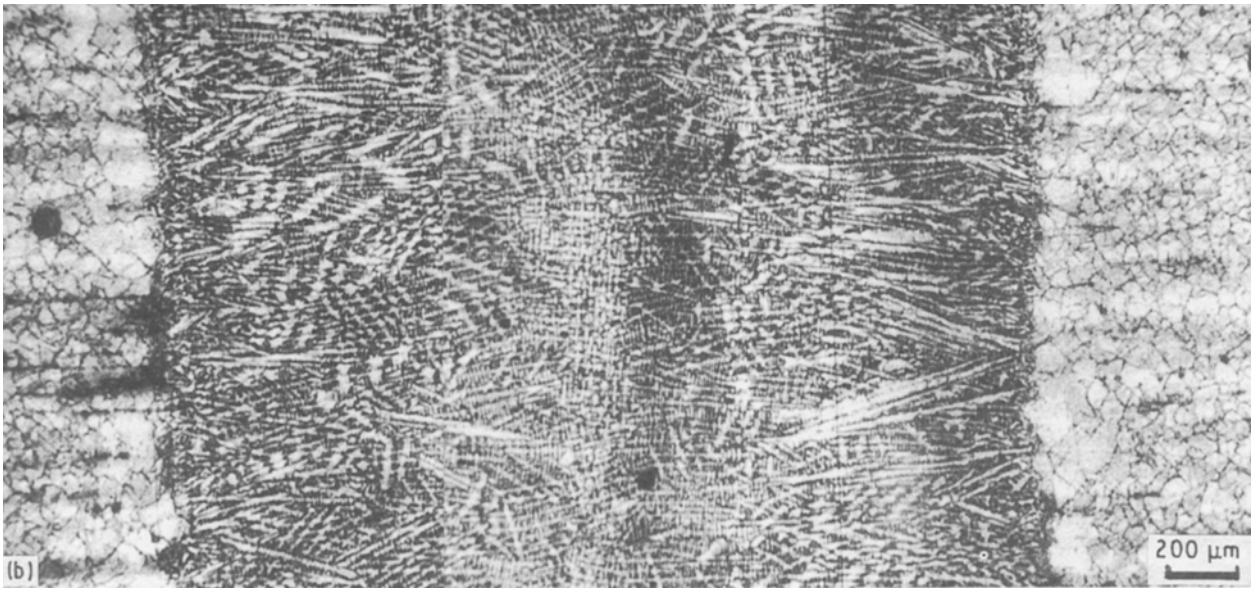

Figure 1 (a) Typical macrostructure of an EB weldment, and (b) microstructure of this weldment.

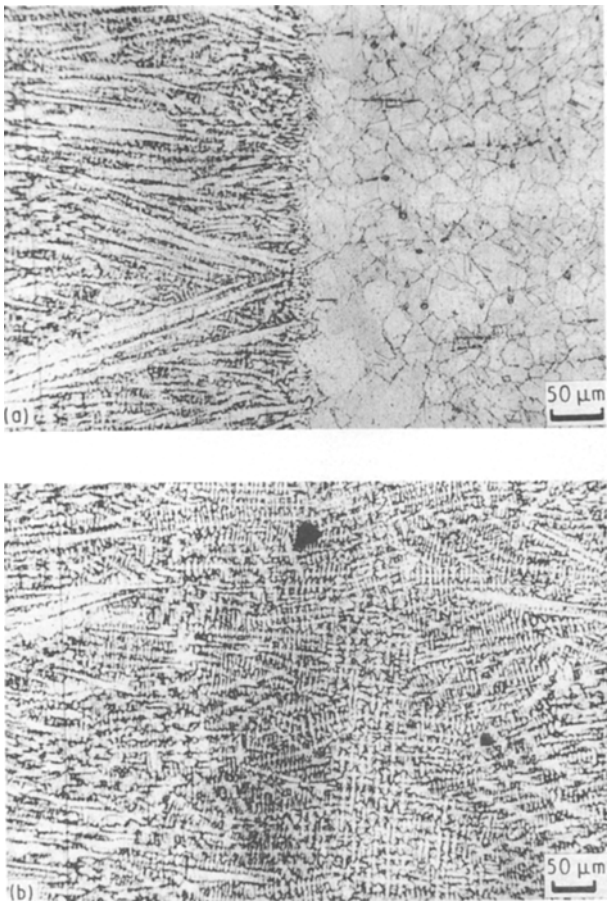

Figure 2 Morphology of austenite in different regions of an EB weldment: (a) columnar morphology at the outer part of the weld pool and (b) equiaxed morphology in the central regions.

ported that K-phase carbide with an $L'1_2$ structure tended to precipitate in the austenitic grain of the Fe–Mn–Al–C alloy during ageing at 500–710 °C for various periods of time [14, 19]. However, a spinodal clustering reaction could have occurred in the Fe–Mn–Al–C alloy during quenching. The spinodally decomposed phase exhibited a modulated structure which grew into a cuboidal phase during ageing treatment [14, 19]. Sun *et al.* [27] reported that rapid cooling does not suppress the formation of spinodally decomposed K-phase in the melt-spun Fe–Mn–Al–C alloy.

In the present work, it is suggested that the K-phase carbide could have precipitated in the austenitic phase of the weld metal during the rapid solidification process produced by welding. Fig. 3a and 3b show the macrostructure and microstructure of the laser welded Fe–28Mn–5Al–1C alloy, respectively. The microstructure of the laser weld is very similar in nature to that described for the EB weld; i.e. it consists mainly of columnar dendrites because high temperature gradients are established between the melt and the bulk. Moreover, the EDX data revealed that a small chemical change had occurred in the Mn content of the weld metal. The dendrite as marked by c in Fig. 3a is composed of 28.48 wt % Mn, 6.73 wt % Al and 64.79 wt % Fe whereas the chemical composition in the position d is 25.43 wt % Mn, 6.70 wt % Al and 67.87 wt % Fe. This chemical change possibly stems from the solute becoming heterogeneous in the molten pool. Several factors are postulated to obtain an homogeneous distribution of solute atoms in the fusion zone; i.e. diffusion of solutes in the melt pool, surface-tension-gradient changes and key-hole steering [28, 29]. Of these factors, the violent agitation of the melt pool by the key-hole stirring effect is believed to be the most important factor in achieving a uniform distribution of alloying elements in the solidified weld metal. Deep key-hole penetration into the fusion zone (Fig. 3a) tends to produce an inhomogeneous distribution of solutes [30]. Moreover, the use of a high-power laser beam can also lead to significant vaporization of some volatile alloying elements, e.g. manganese and magnesium. Khan *et al.* [31] reported that a small reduction in the concentration of manganese is observed at the weld pool during laser-beam welding of high-manganese stainless steel.

3.2. Mechanical properties

3.2.1. Tensile properties

The results of tension tests conducted on the base and weld material are given in Table II. The solution-treated alloy exhibited a higher ultimate tensile strength and ductility (as measured by elongation and reduction in area) than did the EB and laser-welded specimens. However, the weld material was found to have a higher yield strength than the solution-treated alloy. The differences are believed to be due to local microstructural changes produced in the weld metals associated with the EB and laser welding. The tensile specimens fractured at the centre line of the weld metal as expected. Lower ductility values of the laser-welded specimen are possibly due to the laser-welded material exhibiting a larger fusion zone than the EB welded alloy.

3.2.2. Fractography

Fig. 4a shows a low magnification of the SEM fractograph of the EB welded Fe–28Mn–5Al–1C alloy after tensile testing. Higher magnification of the fractographs at the centre and at the edge of this fracture surface are shown in Fig. 4b and c, respectively. The centre of the specimen exhibits ductile dimpled fracture whereas the edge of the specimen fails in a mixed mode, i.e. transgranular cleavage combined with dimpled fracture. The fractographs correlate well with the ductility data of the EB welded alloy listed in Table II which shows that the welded material has lower ductility than the base alloy. The base alloy fails entirely in a ductile dimpled mode.

The fracture pattern of the laser welded Fe–28Mn–5Al–1C alloy exhibits ductile failure and cleavage failure at positions marked by X and Y, respectively, in Fig. 5a. Higher magnification of the fractographs showing ductile and cleavage failure are shown in Fig. 5b and c, respectively. Some small cavities are evident in the cleavage surface shown in Fig. 5c. The cleavage feature apparently tends to reduce the tensile ductility of the laser-welded alloy considerably.

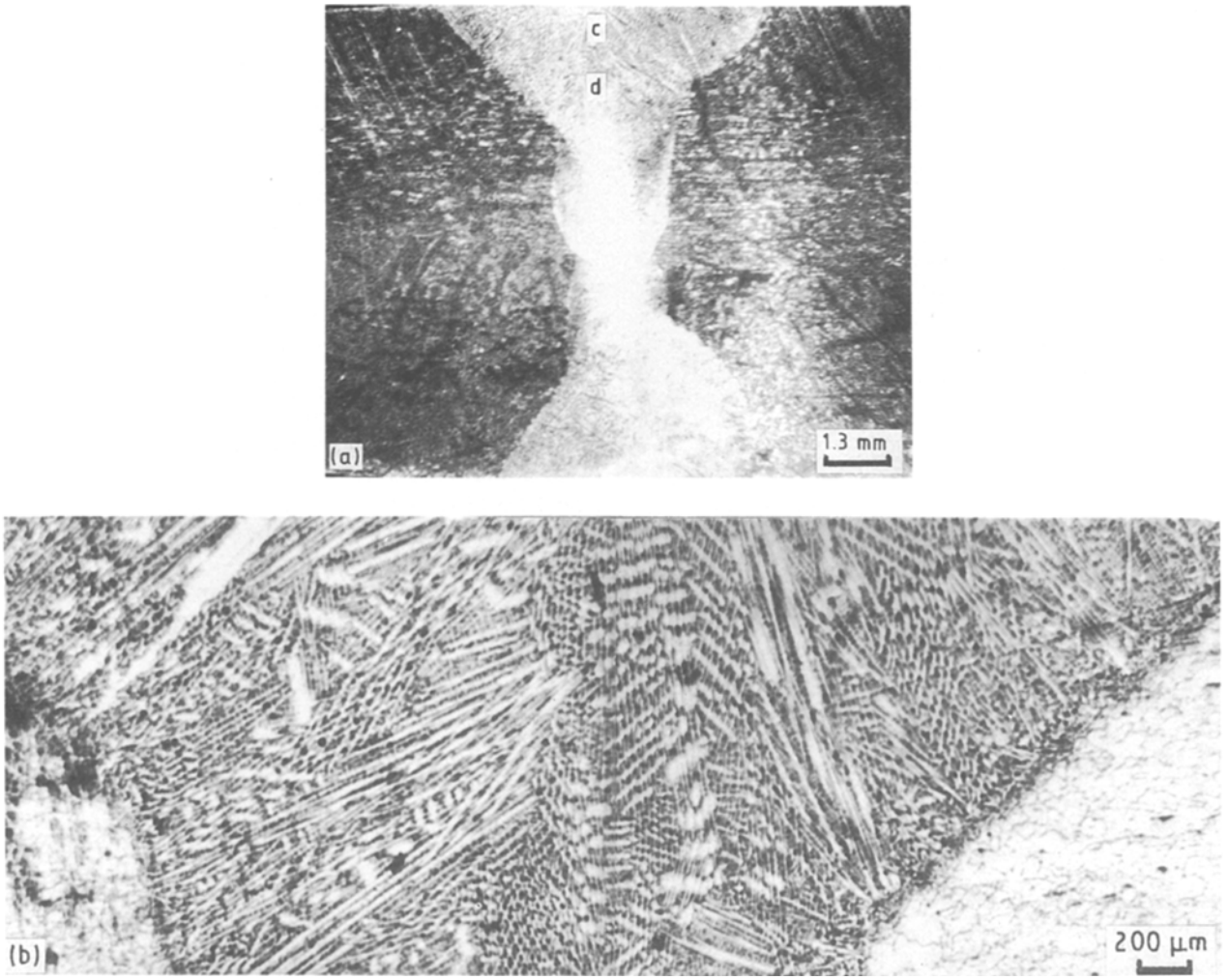

Figure 3 Typical structures of the laser welded Fe–28Mn–5Al–1C alloy: (a) macrostructure and (b) microstructure.

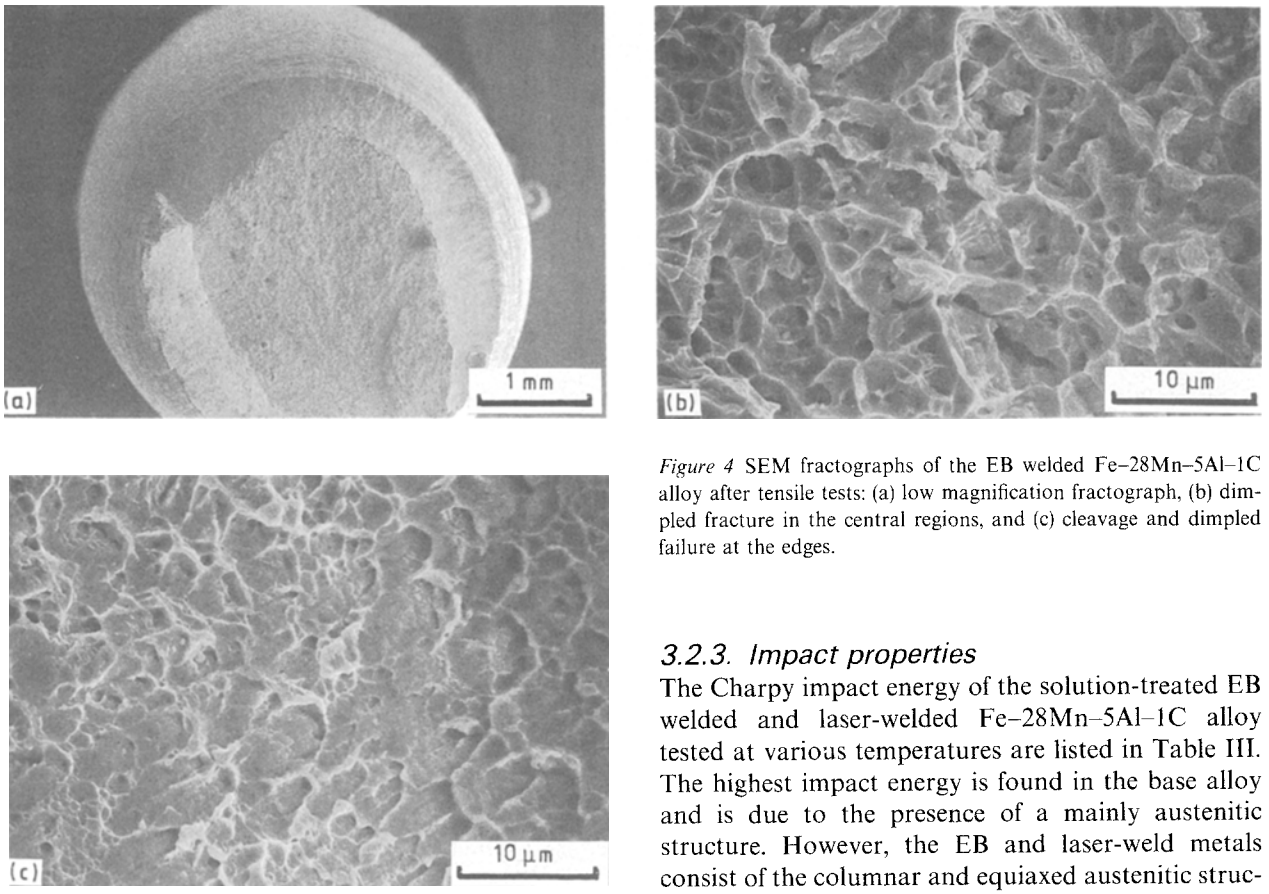

Figure 4 SEM fractographs of the EB welded Fe–28Mn–5Al–1C alloy after tensile tests: (a) low magnification fractograph, (b) dimpled fracture in the central regions, and (c) cleavage and dimpled failure at the edges.

3.2.3. Impact properties

The Charpy impact energy of the solution-treated EB welded and laser-welded Fe–28Mn–5Al–1C alloy tested at various temperatures are listed in Table III. The highest impact energy is found in the base alloy and is due to the presence of a mainly austenitic structure. However, the EB and laser-weld metals consist of the columnar and equiaxed austenitic struc-

TABLE II Tensile properties of solution-treated, EB welded and laser-welded Fe–28Mn–5Al–1C alloy

Material condition	Yield strength (MPa)	Tensile strength (MPa)	Elongation (%)	Reduction in area (%)
Solution treated	535	948	43	55
EB welded	549	930	39.8	27
Laser welded	586	898.4	25	13.2

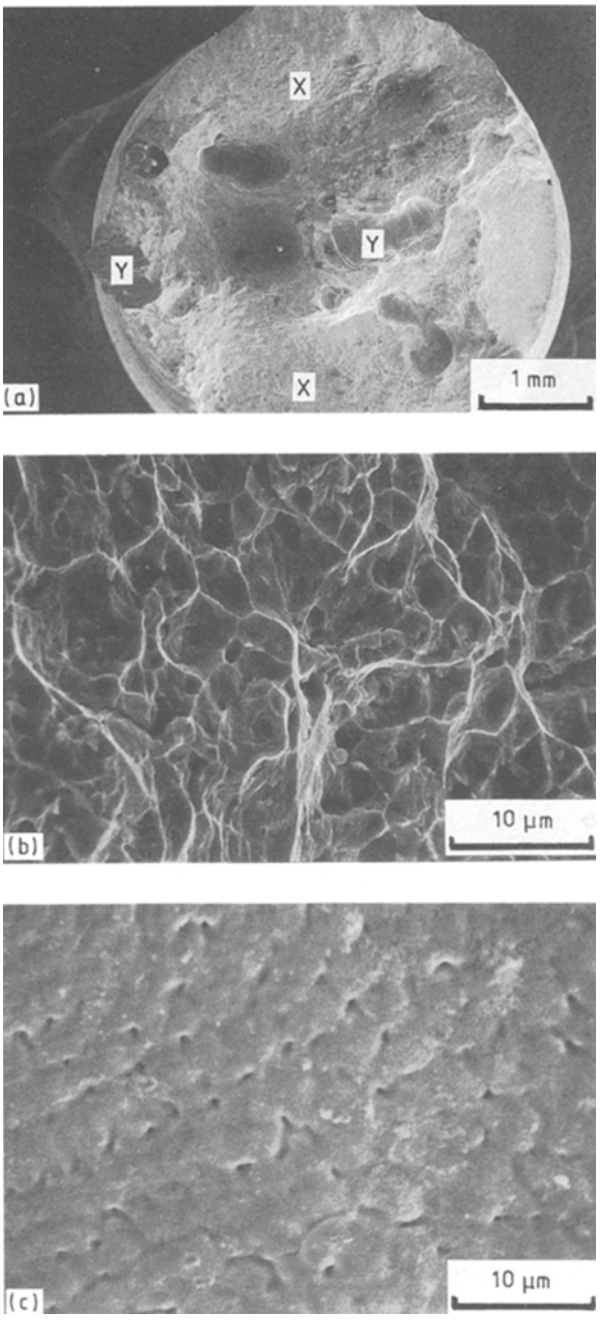

Figure 5 SEM fractographs of the laser-welded Fe–28Mn–5Al–1C alloy after tensile tests: (a) low-magnification fractograph; (b) dimpled fracture in the positions as marked by X in (a), (b) cleavage fracture in the positions as marked by Y in (a).

tures, K-phase carbides and small amounts of ferrite. The impact toughness is affected by a complex combination of the various microstructural phases present in the weldments.

3.3. Corrosion properties

Fig. 6 shows the potentiodynamic curves of the EB and laser-weld metals, and the base alloy exposed in 1N H_2SO_4 solution at 23 °C. The polarization curves exhibit broad active–passive transition peaks and transpassive features. The critical current density for passivation (I_{cp}) and the current density in the passive region (I_{pp}) of the weld metals are higher than those of the base alloy. This is due to the existence of multiphase structures in the weld metals. Fig. 7 shows the polarization curves of the HAZ of the laser weldment and the base alloy exposed in 1M Na_2SO_4 solution at 23 °C. The HAZ is found to have a polarization curve that is virtually identical to that for the base alloy. This is because the phase structure, grain size and chemical composition of the HAZ of the laser weld were found to be similar to those of the base alloy. A typical cyclic polarization curve of the laser weld metal and the base alloy exposed in 1M NaCl solution at 23 °C is shown in Fig. 8. In this figure, one can see that the base alloy exhibits a slightly lower current density in the passive region and also a slightly higher pitting potential. Both weld metal and the base alloy exhibit large hysteresis loops indicating that they are susceptible to pitting and crevice corrosion attack. A similar cyclic polarization behaviour is observed in the EB weld metal exposed in 1M NaCl solution at 23 °C.

TABLE III Charpy Impact energy (J) of solution-treated, EB welded and laser-welded Fe–28Mn–5Al–1C alloy tested at various temperatures

Material condition	23 °C	− 40 °C	− 60 °C	− 196 °C
Solution treated	70.7	43.1	43.0	26.3
EB welded	34.2	20.6	21.7	4.3
Laser welded	32.6	18.2	14.5	2.8

4. Conclusions

1. The optical micrographs reveal that the microstructure of the EB and laser-welded Fe–28Mn–5Al–1C alloy consists mainly of the columnar and equiaxed austenitic structures.

2. The tensile tests show that the weld materials exhibit lower tensile strength and ductility than those of the base alloy.

3. Fractographic analysis reveals that the higher tensile ductility in the EB weld material is mainly associated with a microvoid coalescence mode of failure, giving rise to dimple formation at the central region of the specimen. However, the cleavage pattern together with some finer dimples are found to be present at the edges of the fracture surface.

4. The impact properties of the weld materials, especially the laser-welded alloy, are inferior to those

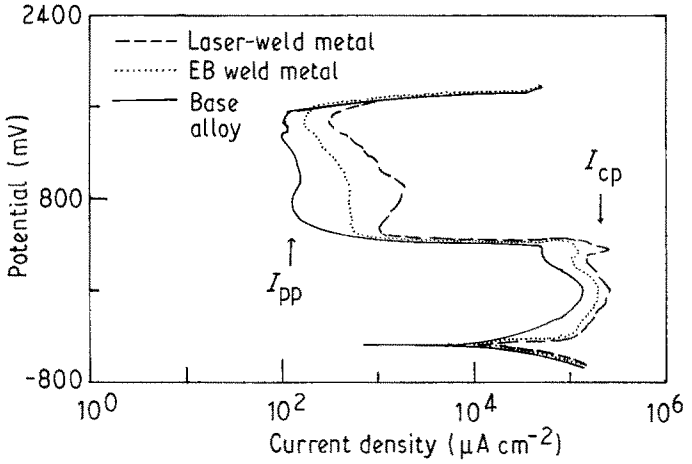

Figure 6 Potentiodynamic curves of the base alloy, EB and laser-weld metals exposed in 1N H_2SO_4 solution at 23 °C.

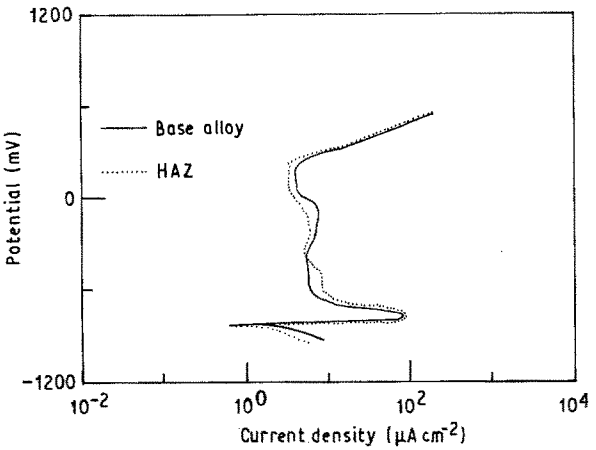

Figure 7 Potentiodynamic curves of the HAZ of the laser weldment and the base alloy exposed in 1M Na_2SO_4 solution at 23 °C.

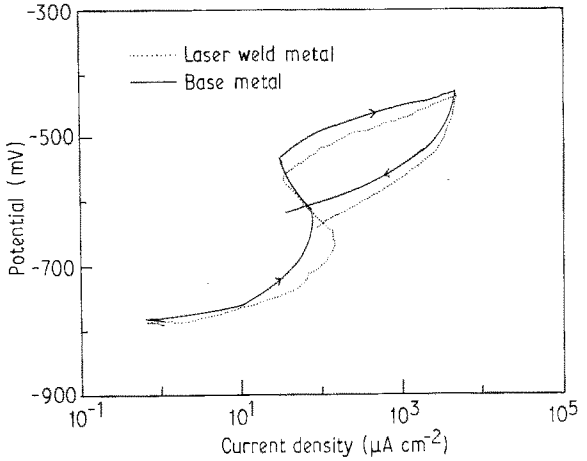

Figure 8 Cyclic polarization curves of the laser-weld metal and the base alloy exposed in 1M NaCl solution at 23 °C.

of the base alloy. This is due to the presence of multiphase structures in the EB and laser weldments.

5. The anodic polarization behaviour of the HAZ of the weld material is identical to that of the base alloy when exposed in 1M Na_2SO_4 solution at 23 °C. However, the EB and laser-weld metals exhibit higher current density in the passive region and critical current density for passivation than those of the base alloy when exposed in 1N H_2SO_4 solution at 23 °C.

References

1. J. J. HEGER, ASTM STP 369, Philadelphia (1965) 54.
2. J. W. FOURIE and A. P. BENTLEY, in "High manganese austenitic steels", edited by R. A. Lula (American Society for Metals, Metals Park, 1987) 111.
3. W. C. J. VAN RENSBURG, in "Strategic Materials", (Prentice-Hall Inc., Englewood Cliffs, 1986) 116.
4. S. C. TJONG, *Trans. J.I.M.* **28** (1987) 671.
5. J. P. SAUER, R. A. RAPP and J. P. HIRTH, *Oxid. Met.* **18** (1982) 285.
6. S. C. TJONG, *X-ray Spectrom.* **20** (1991) 225.
7. J. E. KRZANOWSKI, *Met. Trans.* **19A** (1988) 1873.
8. S. C. TJONG, *Surf. Coat. Technol.* **28** (1986) 181.
9. G. L. KAYAK, *Met. Sci. Heat Treat.* **2** (1969) 95.
10. S. C. TJONG, *Steel Res.* **59** (1988) 499.
11. S. C. TJONG, *Steel Res.* **60** (1989) 91.
12. S. C. TJONG and H. C. SWART, *Appl. Surf. Sci.* **47** (1991) 311.
13. S. C. TJONG, *Werks. Korros.* **37** (1986) 444.
14. S. C. TJONG and C. S. WU, *Mater. Sci. Engng.* **80** (1986) 203.
15. S. C. TJONG, *J. Mater. Sci.* **21** (1986) 1166.
16. N. J. HO, C. M. CHEN and S. C. TJONG, *Scripta Metall.* **21** (1987) 1319.
17. S. C. TJONG and N. J. HO, *Mater. Sci. Engng.* **91** (1987) 161.
18. N. J. HO and S. C. TJONG, *Mater. Sci. Engng.* **94** (1987) 195.
19. S. C. TJONG, *Mater. Charact.* **24** (1990) 275.
20. D. K. AIDUN and J. SUH, *Steel Res.* **58** (1987) 528.
21. A. K. LIPPERT and D. K. AIDUN, *Weld. J.* **66** (1987) 29.
22. C. P. CHOU and C. H. LEE, *Met. Trans.* **20A** (1989) 2559.
23. C. P. CHOU and C. H. LEE, *Scripta Metall.* **23** (1989) 1109.
24. C. P. CHOU and C. H. LEE, *J. Mater. Sci.* **25** (1990) 1491.
25. W. F. SAVAGE, C. D. LUNDIN and A. H. OLSON, *Weld. J.* **44** (1965) 1s.
26. C. P. CHOU and C. H. LEE, *Scripta Metall.* **23** (1989) 901.
27. Z. SUN, H. A. DAVIES and J. A. WHITEMAN, *Met. Sci.* **18** (1984) 459.
28. L. S. WEINMAN and J. N. DEVAULT, in proceedings of Laser-Solid Interactions and Laser Processing, edited by S. D. Ferris, H. T. Leamy and J. M. Poate, Boston, Amer. Inst. Phys., New York (1978) 239.
29. T. R. ANTHONY and H. E. CLINE, *J. Appl. Phys.* **48** (1977) 3888.
30. P. A. MOLIAN, *Scripta Metall.* **16** (1982) 65.
31. P. A. KHAN, T. DEBROY and S. A. DAVID, *Welding J.* **67** (1988) 1s.

Received 4 march
and accepted 14 September